Supplementary Information (SI) for Journal of Materials Chemistry A.
This journal is © The Royal Society of Chemistry 2026

Phosphonitrile-based Porous Polymer Interfaces for Coupled Homogenization of Zn^{2+} Flux and Interfacial Electric Field Distribution Enabling Dendrite-free Zinc Anodes

Lei-Guo Li [a, b], Wei-Hai Yi [a, b], Wen-Jie Shi [a, b], Xin-Ying Ren [a, b], Min-Peng Li [a, b], Meng-Chao Liu [a, b], Ming-Hui Yang [a, b], Hong-Yan Li [a, b], and Mao-Cheng Liu [a, b] *

[a] State Key Laboratory of Advanced Processing and Recycling of Non-ferrous Metals, Lanzhou University of Technology, Lanzhou 730050, People's Republic of China

[b] School of Materials Science and Engineering, Lanzhou University of Technology, Lanzhou 730050, People's Republic of China

Chemicals and Materials

Phosphonitrilic chloride trimer ($N_3P_3Cl_6$, 98%), *p*-hydroxybenzaldehyde (AR), m-Phenylenediamine (m-PD, 98%), ammonium metavanadate (NH_4VO_3, ≥99.9%), and citric acid ($C_6H_8O_7$, ≥99.5%)were purchased from Shanghai Aladdin Biochemical Technology Co., Ltd. (Shanghai, China). Dimethyl sulfoxide (DMSO), tetrahydrofuran (THF), potassium carbonate (K_2CO_3), N-methylpyrrolidone (NMP), and acetone were obtained from Sinopharm Chemical Reagent Co., Ltd. (China). All chemicals were used as received without further purification.

Synthesis of HAPCP and PPOP

$N_3P_3Cl_6$ (2.09 g, 6.0 mmol) and *p*-hydroxybenzaldehyde (4.5 g, 36.8 mmol) were added sequentially to a 50 mL THF solution containing K_2CO_3 (10 g, 10.8 mmol). The mixture was heated to 50 °C and stirred under a nitrogen atmosphere for 3 days. After cooling to room temperature, 100 mL of water was added, and the reaction mixture was stirred for an additional 3 h at room temperature. The resulting precipitate was collected by filtration, washed thoroughly with water until it turned white, and dried under reduced pressure at 60 °C for 48 h to yield the hexakis (4-formylphenoxy) cyclotriphosphazene (HAPCP) monomer in 90% yield.

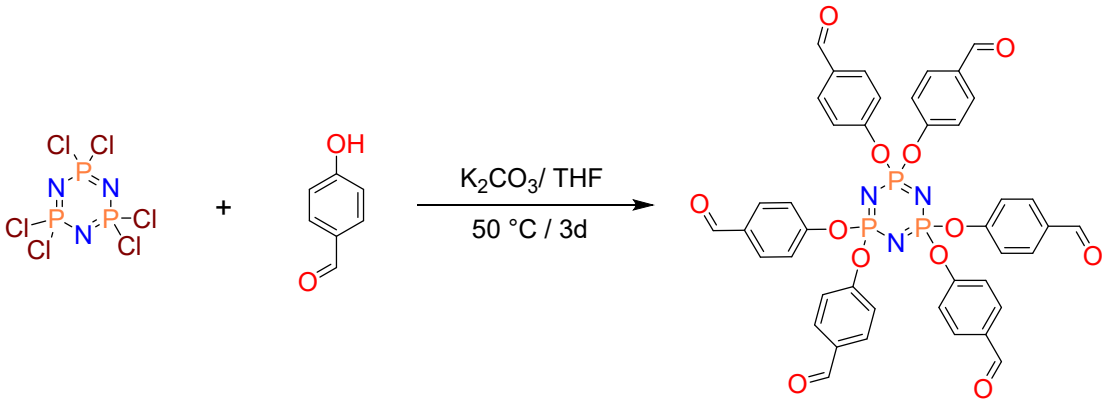

Scheme S1: Schematic illustration of the synthetic routes of HAPCP [$N_3P_3(OC_6H_4CHO)_6$]

Under a nitrogen atmosphere, HAPCP (400 mg) and DMSO (4.0 mL) were added to a 25 mL reaction vessel. After stirring for 5 min, the m-PD (150.7 mg) dissolved in DMSO (2 mL) was introduced at a rate of 0.05 mL min^{-1} at 50 °C using a syringe pump over 45 min. The oil-bath temperature was then gradually increased to 160 °C over 20 min. After the nitrogen flow stopped, the system remained under a nitrogen atmosphere. When the oil bath reached 160 °C, reflux became visible inside the flask, and bright yellow to dark-brown solid precipitates typically formed within 10–30 min. The reaction was maintained at 160 °C under nitrogen for an additional 24 h. Upon completion, the mixture was cooled to room temperature, filtered, and washed three times with anhydrous tetrahydrofuran, followed by Soxhlet extraction with THF for 24 h. The final product was dried under vacuum at 60 °C for 24 h to obtain PPOP solid, being ground with a mortar and pestle into a fine powder.

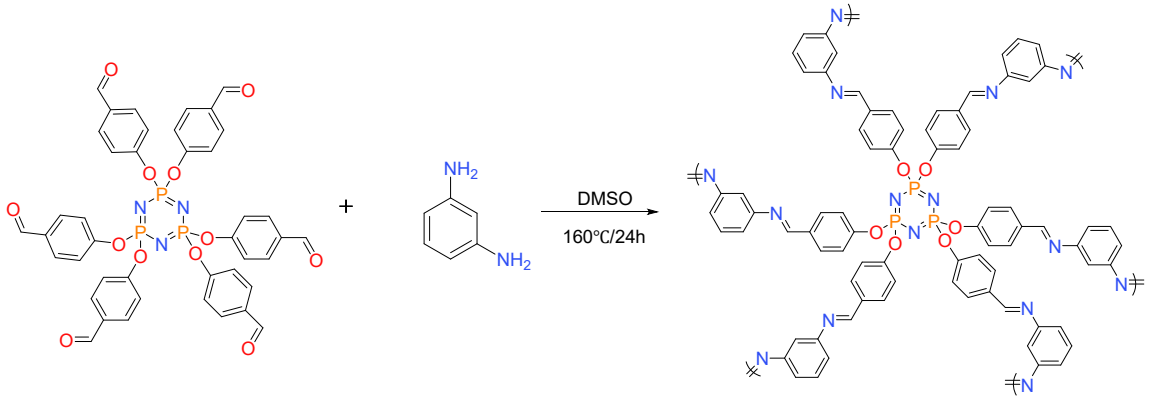

Scheme S2: Schematic illustration of the synthetic routes of PPOP

Synthesis of ammonium vanadate (NVO).

2.632 g of NH_4VO_3 was dissolved in 90 mL of deionized water, then 4.323 g of $C_6H_8O_7$ was added. The mixture was stirred in a 70°C water bath for 30 minutes and then transferred to a 150 mL teffon

lined autoclave and heated at 180°C for 10 h. After natural cooling to room temperature, the resulting precipitate was separated by centrifugation and washed three times with deionized water and ethanol. The final product was dried at 80°C for 12 h to obtain an NVO sample.

Fabrication of PPOP@Zn anode

Commercial zinc foil (thickness: 0.02 mm, Zn content ≥ 99.9%) was used as the substrate for fabricating the Zn anode. A homogeneous slurry was prepared by mixing 90 mg of the N/P-doped porous polymer (PPOP), 10 mg of polyvinylidene fluoride (PVDF) as a binder, and NMP (0.5 mL) as the dispersing solvent. The resulting slurry was uniformly cast onto the exposed surface of the zinc foil and subsequently dried in an vacuum oven at 70 °C for 24 h to obtain the PPOP@Zn anode.

Material characterizations

X-ray diffraction (XRD) patterns were recorded on a Rigaku Mini Flex 600 diffractometer using Cu Kα-radiation (0.15406 nm). Morphology images were collected on a field emission scanning electron microscope (FESEM, FEI Nova NanoSEM 230, 10 kV). Analysis of the chemical state of the elements in the samples by X-ray photoelectron spectroscopy (XPS) using the ESCALAB 250Xi model. Fourier transform infrared (FT-IR) was tested to discover the appearance of a new chemical bond in HAPCP and PPOP. Chemical structure analysis via Raman spectroscopy (Auspectrum Tiancheng ATR8800s). The contact angle between the electrolyte and the Zn electrode was measured by a contact angle measuring instrument (JC2000D1, Shanghai Power each Digital Technology Equipment Co, Ltd).

Electrochemical measurements

All electrochemical measurements were carried out under ambient conditions using CR2032 coin cells. The synthesized PPOP@Zn electrodes (Φ = 14 mm) were employed as the anodes, glass fiber membranes (GF/D, Whatman) were used as separators, and 2 M $ZnSO_4$ aqueous solution (100 μL) served as the electrolyte to assemble symmetrical battery. For the full cells, the cathode slurry was prepared by mixing NVO powder, Super P, and PVDF at a mass ratio of 7:2:1 in NMP. The slurry was cast onto titanium foil using a doctor blade and dried in a vacuum oven at 60 °C for 24 h. All battery assembly is performed in an air-free environment. In the PPOP@Zn||NVO full battery, NVO was used as the cathode material, and 2.0 M $ZnSO_4$ aqueous solution was employed as the electrolyte. A three-electrode system (PPOP@Zn working electrode, SCE reference, Pt counter) was used for

linear polarization measurements in 1 M Na_2SO_4; corrosion parameters were derived via Tafel extrapolation on a CHI760E electrochemical workstation (Chenhua, Shanghai), which was also employed for Cyclic voltammetry (CV), electrochemical impedance spectroscopy (EIS) and linear sweep voltammetry (LSV) tests. Galvanostatic charge–discharge cycling tests were conducted at room temperature using a LAND battery testing system (CT2001A, China).

EIS are recorded from 293.15 K to 333.15 K with the Arrhenius equation (1) to calculate Ea.

$$R_{ct} = A * \exp\left(\frac{E_a}{RT}\right) \quad (1)$$

where Rct is the interface resistance, A is the frequency factor, R is the gas constant, and T is the absolute temperature.

The Zn^{2+} transfer numbers are evaluated utilizing symmetric cells combined by EIS before and after the chronoamperometry (CA) test, and they are calculated by the following equation (2).

$$t_{zn^{2+}} = \frac{I_s(\Delta V - I_0 R_0)}{I_0(\Delta V - I_s R_s)} \quad (2)$$

where ΔV is the constant polarization voltage applied (20 mV), R_0 and I_0 are the initial resistance and current, and Rs and Is are the resistance and steady-state current, respectively.

The exchange current density related to the Zn electrodeposition process at various current densities can be calculated from equation (3).

$$i = i_0 \frac{2F}{RT} \eta \quad (3)$$

where i is running current density, i_0 represents the exchange current density, F and R are the Faraday constant and the gas constant, respectively, T is the absolute temperature, and η corresponds to the total overpotential.

The electric double-layer capacitance (EDLC) value was calculated by the equation as follows:

$$c = \frac{i}{v} \quad (4)$$

where C means the capacitance, i corresponds to the current and was defined by half of the difference between positive and negative scanning current at each scanning rate.

Density functional theory (DFT) calculations

First-principles calculations based on density functional theory (DFT) were used to determine the key

thermodynamic parameters. All calculations were performed using the Vienna ab initio simulation package (VASP). The electron-ion interaction was described by the projector augmented wave (PAW) method, and the exchange-correlation functional was treated with the generalized gradient approximation (GGA) using the Perdew-Burke-Ernzerhof (PBE) parameterization scheme. The empirical dispersion correction using the DFT-D3 method of Grimme was employed to describe the van der Waals interactions accurately. A plane-wave energy cutoff of 520 eV was used. For structural optimization, the Brillouin zone was sampled with a Monkhorst–Pack 2×2×1 k-point mesh. The geometric structure was fully relaxed until the force on each atom was less than 0.03 eV $Å^{-1}$ and the energy convergence criterion was set to 10^{-4} eV. Additionally, a 15 Å vacuum layer was applied along the direction perpendicular to the Zn substrate to mitigate interactions between periodic images. The climbing image nudged elastic band (CI-NEB) method was employed to locate the transition states along key reaction pathways. Four intermediate images were used, and the calculations converged when the residual forces on all atoms fell below 0.03 eV $Å^{-1}$, thus ensuring the accurate identification of first-order saddle points.

The binding energy (Eads) was calculated according to:

$$E_{ads} = E_{total} - E_{Zn^{2+}} - E_{PPOP}$$

where E_{total} is the total energy of the adsorption system, $E_{Zn^{2+}}$, and E_{PPOP} represent the energies of the Zn^{2+}, and the PPOP layer structure, respectively.

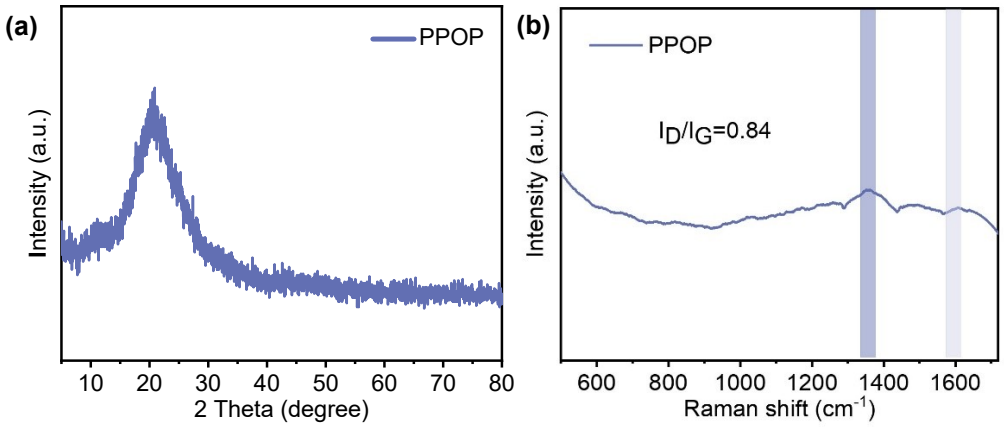

Figure S1. a) XRD patterns of PPOP powder. b) Raman spectrum of PPOP.

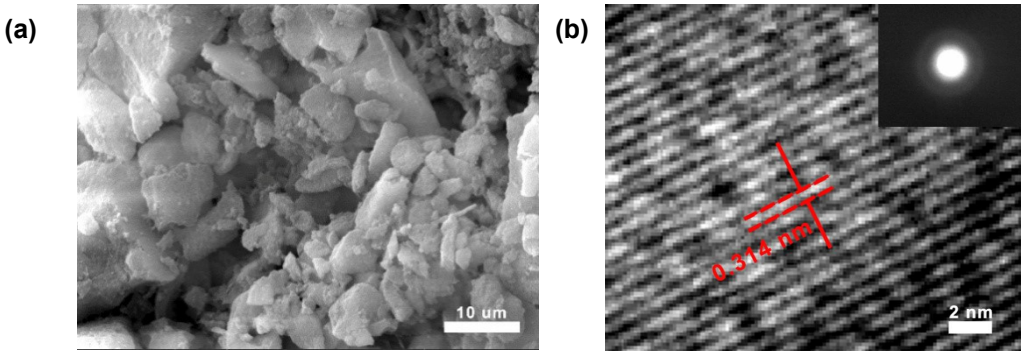

Figure S2. a) SEM images of Zn foil coated with PPOP. b) TEM image of PPOP.

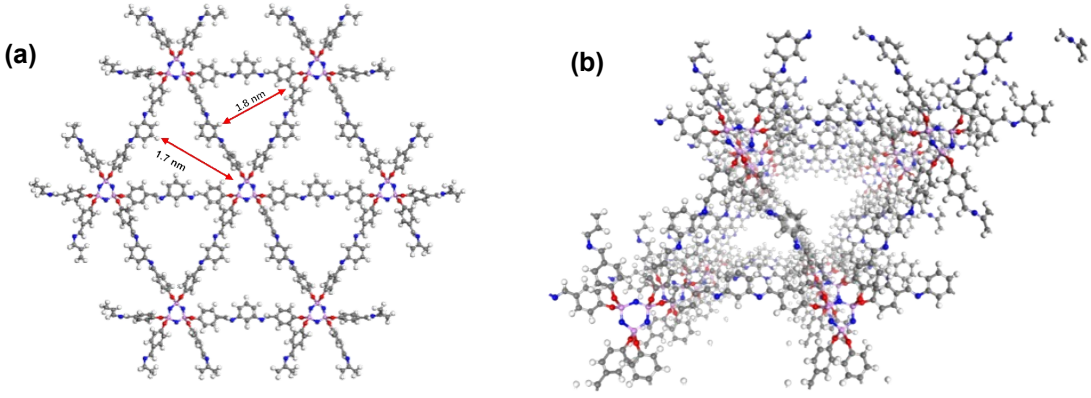

Figure S3. The simulated structure of PPOP with a) ion transport nanochannels b) 3D aperture distribution.

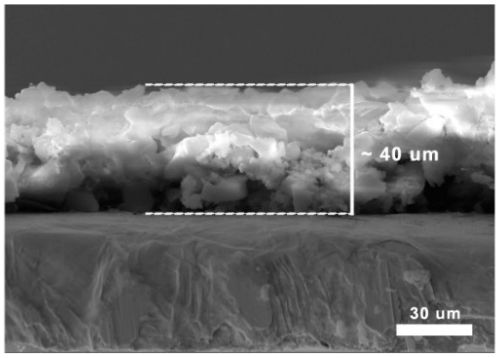

Figure S4. SEM image of the Cross-sectional view of the PPOP layer.

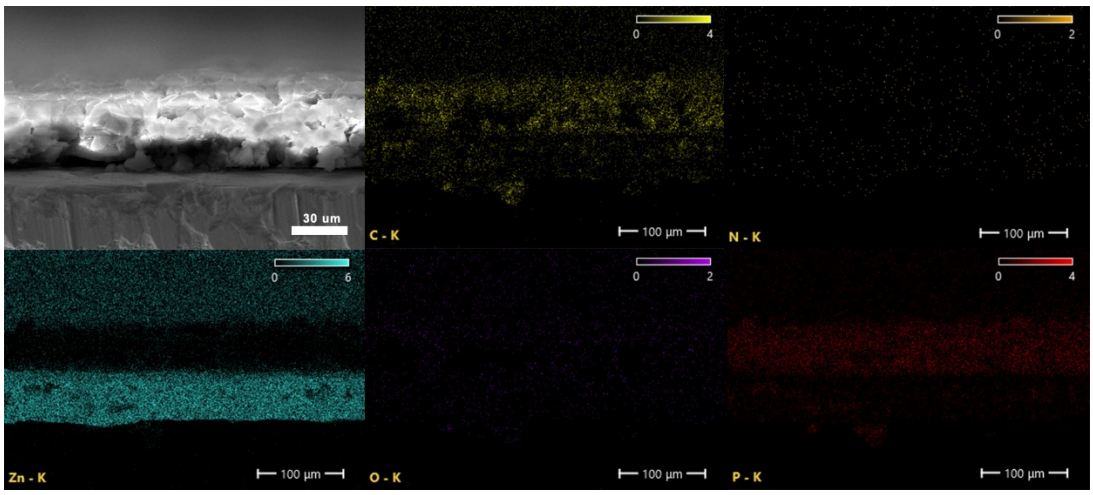

Figure S5. EDS mapping of C, P, O, N and Zn element distribution of the PPOP.

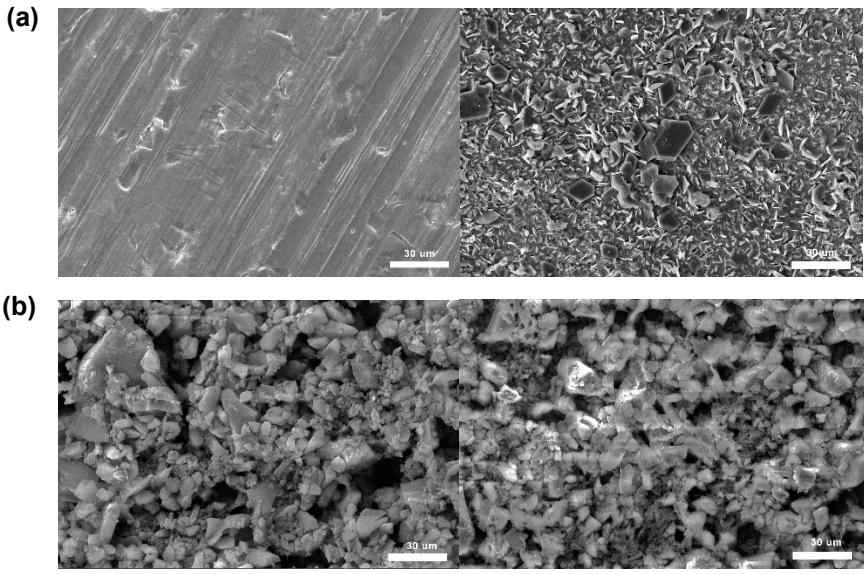

Figure S6. SEM image of Bare Zn and PPOP@Zn after immersion in 2 M $ZnSO_4$ electrolyte for 7 days.

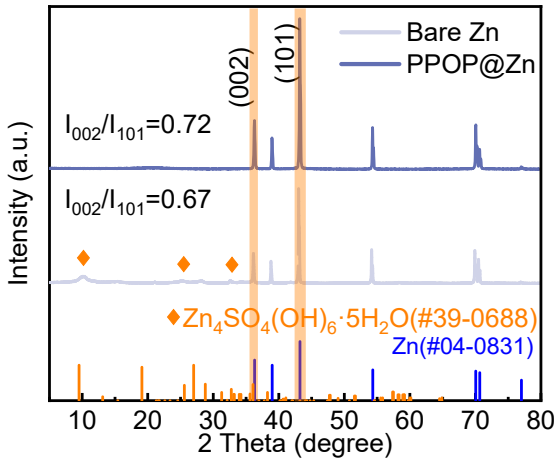

Figure S7. XRD patterns of Bare Zn and PPOP@Zn anodes after 200 cycles at 2 mA cm^{-2}.

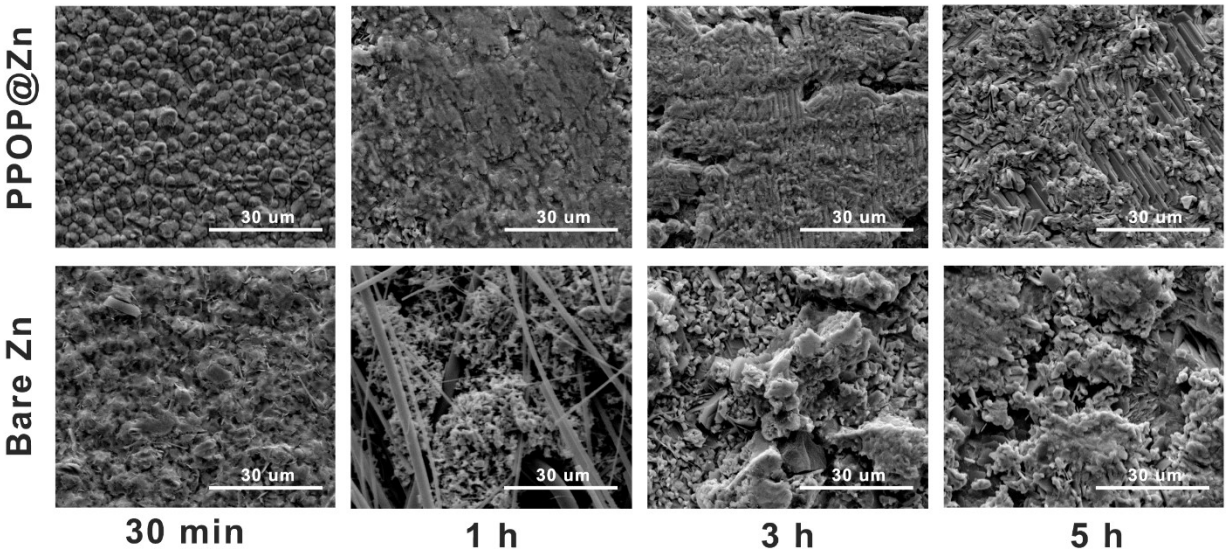

Figure S8. SEM image of PPOP@Zn and bare Zn anodes after deposition for 30 min, 1, 3, and 5 h at 1 mA cm^{-2}.

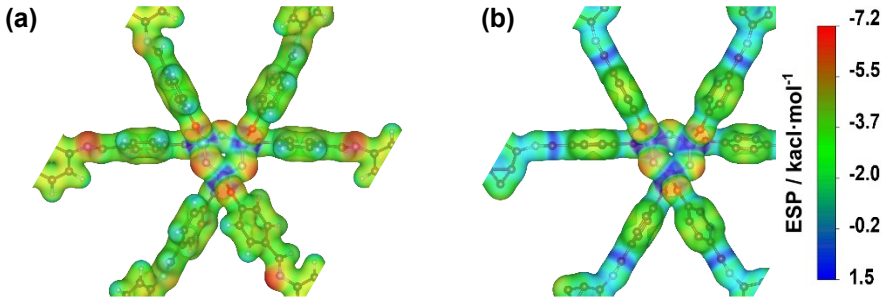

Figure S9. Electrostatic potential (ESP) distribution diagrams of a) PPOP b) Zn^{2+} at site 1 in PPOP molecules.

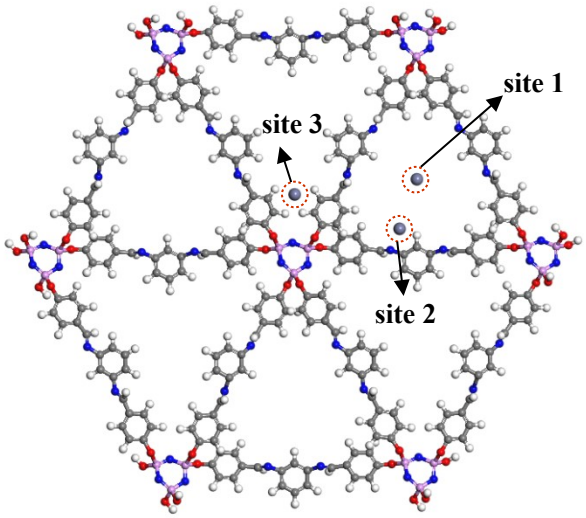

Figure S10. Adsorption energy of Zn^{2+} at different positions in PPOP.

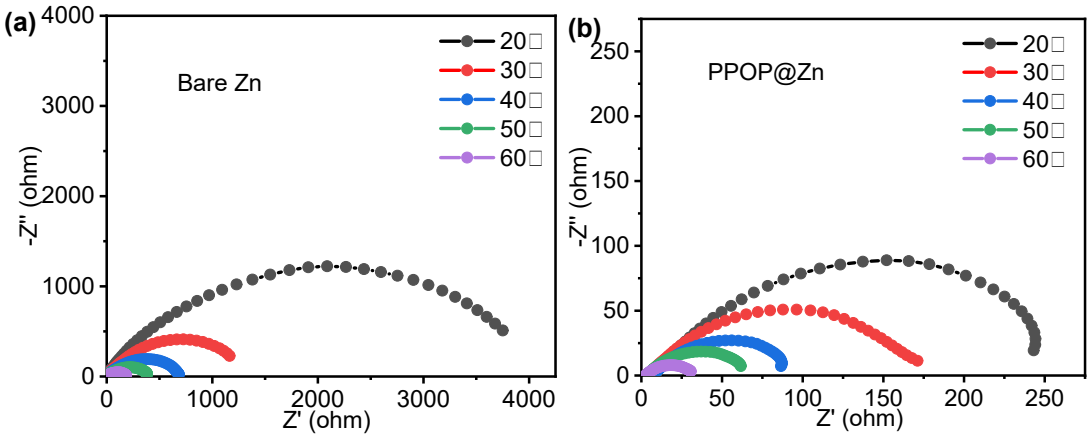

Figure S11. EIS of a) Bare-Zn, b) PPOP@Zn symmetric batteries at different temperatures.

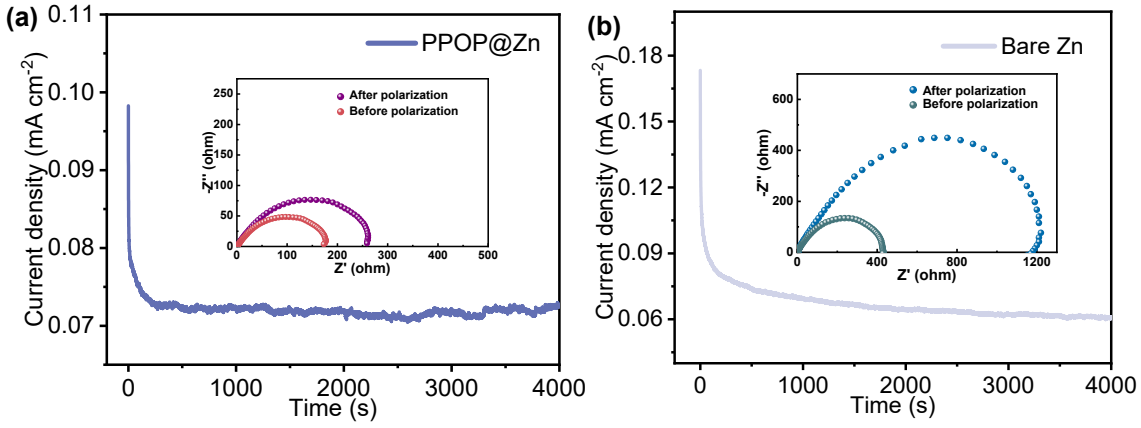

Figure S12. Current-time curves of Zn symmetric cells assembled with a) bare-Zn and b) PPOP@Zn under constant voltage (10 mV) polarization. The insets are the impedance spectra before and after polarization, respectively.

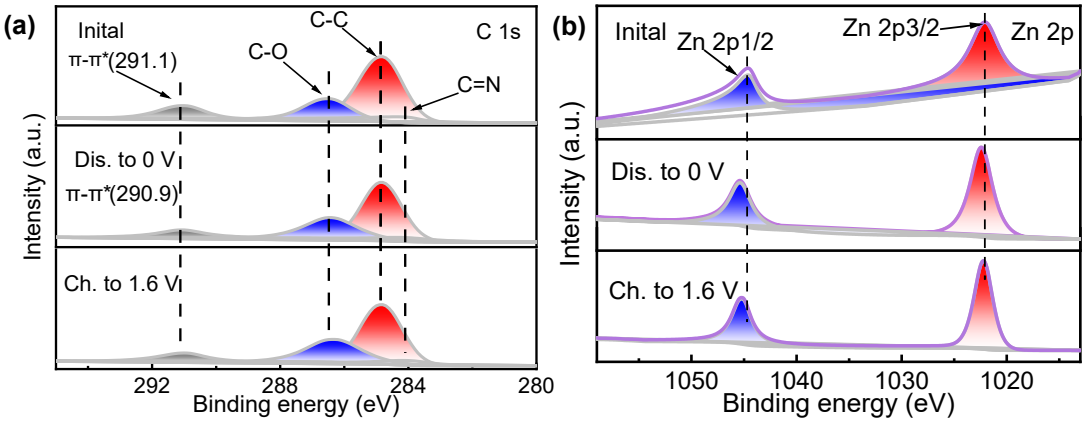

Figure S13. The corresponding a) C 1s and b) Zn 2p spectra of the ex-situ XPS analysis.

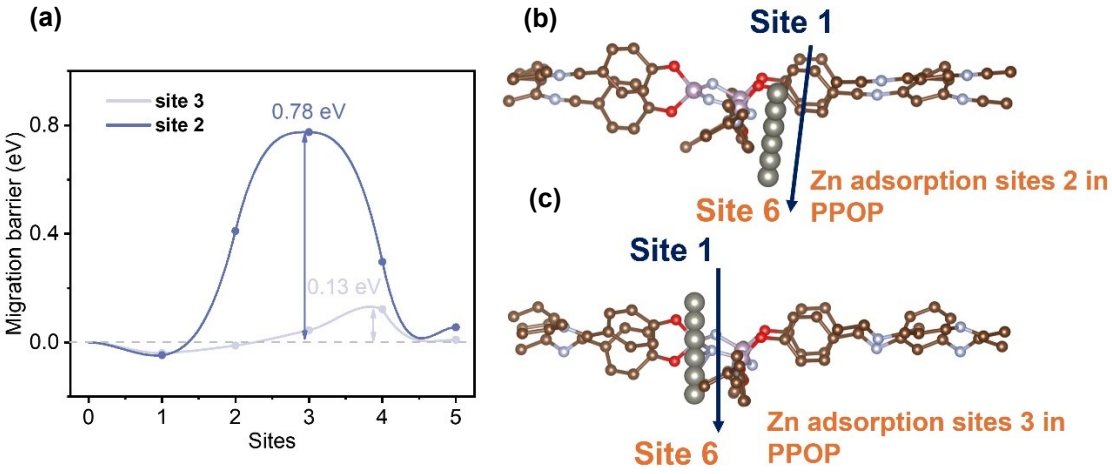

Figure S14. (a) Migration barrier of Zn^{2+} diffusion on the interlayer of Site 2 and Site 3 in PPOP. Zn^{2+} diffusion path in the interlayers of (b) Site 2 and (c) Site 3.

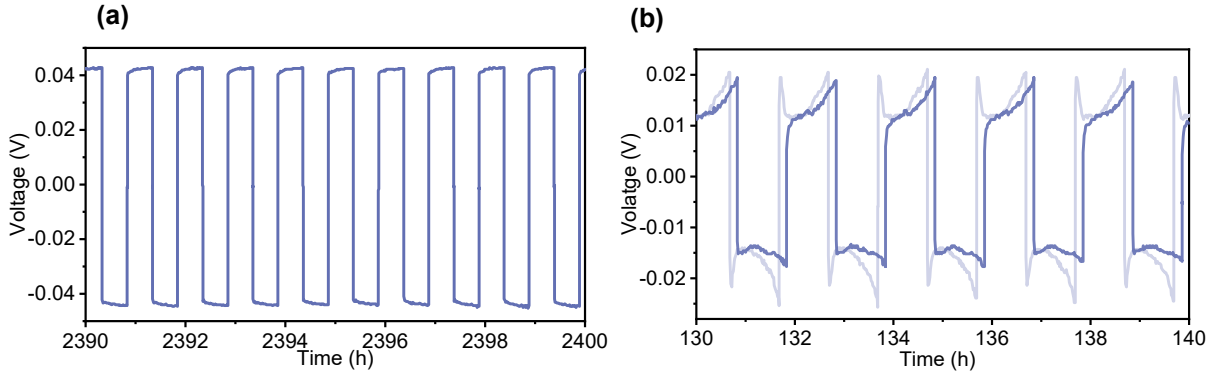

Figure S15. The magnified voltage curves of PPOP@Zn symmetric battery at 2400 h in Figure a) and shows a small polarization voltage in Figure b)

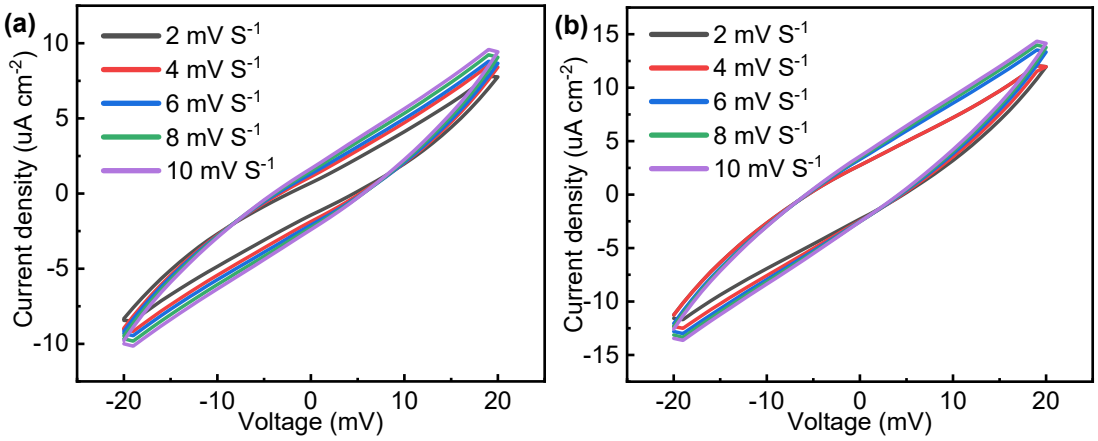

Figure S16. Electric double-layer capacitance (EDLC) measurements for a) bare Zn and b) PPOP@Zn. CV curves for Zn||Zn symmetric cells in a voltage range from -20 mV to 20 mV under various scanning rates.

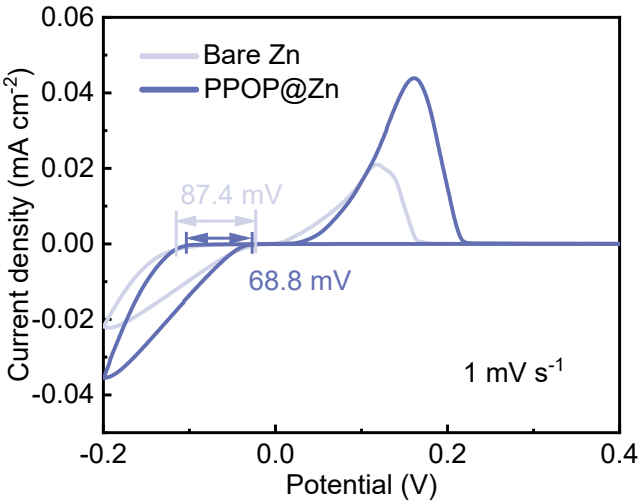

Figure S17. CV curves of Zn||Cu and PPOP@Zn||Cu asymmetric batteries.

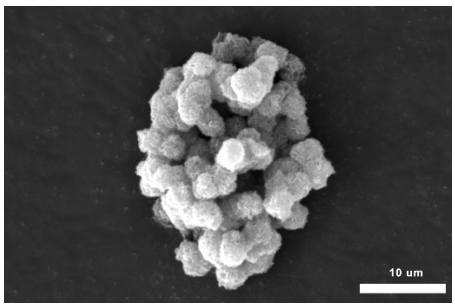

Figure S18. SEM image of NVO powders.

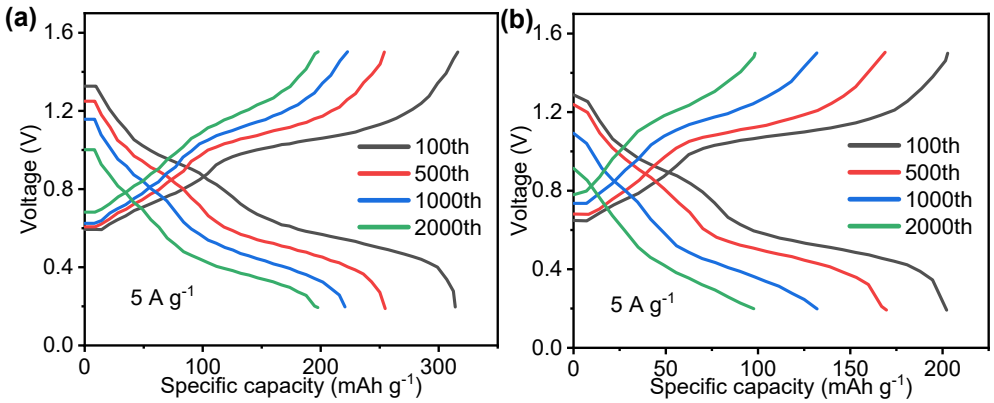

Figure S19. charge-discharge curves of PPOP@Zn||NVO and Zn||NVO full cells at 5 A g^{-1}.

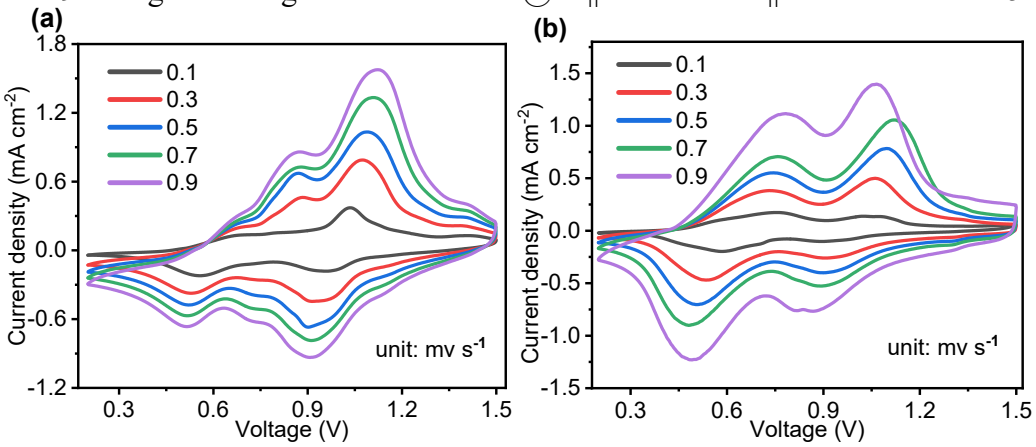

Figure S20. CV curve of PPOP@Zn and bare Zn full batteries at different scan rate.

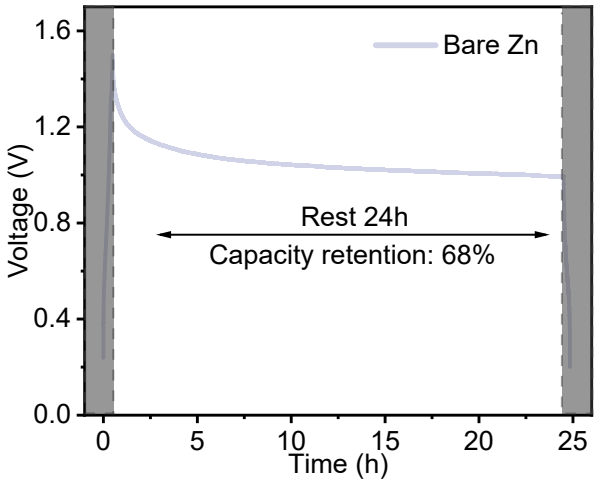

Figure S21. Charge–discharge curves of Zn||NVO full batteries.

Table S1. Comparison of the key Zn-anode performance metrics of PPOP@Zn with recent representative studies[1-9].

Strategy	Current density (mA cm^{-2})	Areal capacity (mAh cm^{-2})	Cycling life (h)	CE (%)	Ref.
PPOP@Zn	5	2.5	＞1800	99.60	This work
Literature 1	0.5	0.5	1250	99.80	Ref.1
Literature 2	5	1	2000	99.31	Ref.2
Literature 3	1	0.498	870	99.96	Ref.3
Literature 4	25	1	＞34390	99.91	Ref.4
Literature 5	10	1	＞800	97.8	Ref.5
Literature 6	20	20	＞400	99.90	Ref.6
Literature 7	1	1	5500	99.50	Ref.7
Literature 8	0.5	0.25	1800	99.80	Ref.8
Literature 9	0.5	0.25	2200	99.70	Ref.9

Reference

[1] X.-Y. Ren, M.-P. Li, W.-J. Shi, W.-H. Yi, H.-Y. Li, C.-X. Zheng, X.-R. Wang, M.-C. Liu, Y.-X. Hu, Surface engineering of amide-functionalized microporous polymers for enhanced zincophilicity and dendrite-free zinc anodes, Journal of Energy Storage (2025). https://doi.org/10.1016/j.est.2025.118872.

[2] W.-H. Yi, W.-J. Shi, M.-P. Li, H.-Y. Li, C.-X. Zheng, X.-Y. Ren, Q. Zhou, M.-C. Liu, Synergistic ion adsorption and electron transfer in porphyrin-based conjugated microporous polymers enabling stable Zn anodes, Chemical Engineering Journal (2025). https://doi.org/10.1016/j.cej.2025.167625.

[3] P. Sintipditsakul, C. Yang, Z. Dai, N. Kiatwisarnkij, K. Lolupiman, P. Woottapanit, X. Zhang, P. Wangyao, J. Qin, Construction of Artificial Interface Layer in the Fly Ash Suspension for Durable Zn Anode, ACS Applied Energy Materials (2025). https://doi.org/10.1021/acsaem.4c02966.

[4] C. Yuan, C. Wang, D. Guo, J. Zhang, J. Sun, S. Tian, H. Lu, H. Quan, X. Zhan, C. Sun, S. Wang, Colloid size engineering enables ultra-stable Zn anodes via electrokinetic and interfacial regulation, Chemical Engineering Journal (2026). https://doi.org/10.1016/j.cej.2026.174400.

[5] C. Yuan, J. Xiao, C. Liu, X. Zhan, Elucidating synergistic mechanisms of an anion–cation electrolyte additive for ultra-stable zinc metal anodes, Journal of Materials Chemistry A (2024). https://doi.org/10.1039/d4ta03414g.

[6] X. Sun, X. Zhan, C. Wu, Z. Gu, W. Han, H. Zhang, L. Zhu, Mechanistic Insights into Dendrite Growth in Aqueous Zinc-Ion Batteries with Trace Propylene Carbonate Electrolyte Additive, ACS Energy Letters (2026). https://doi.org/10.1021/acsenergylett.5c04147.

[7] C. Yang, P. Woottapanit, S. Geng, R. Chanajaree, K. Lolupiman, W. Limphirat, X. Zhang, J. Qin, Biomimetic Inorganic–Organic Protective Layer for Highly Stable and Reversible Zn Anodes, ACS Energy Letters (2024). https://doi.org/10.1021/acsenergylett.4c03005.

[8] P. Tanapornchinpong, C.-W. Yang, Y.-H. Zhao, N. Kiatwisarnkij, K. Lolupiman, S. Rajendran, Y.-P. Lei, X.-Y. Zhang, P. Wangyao, J.-Q. Qin, Enhanced Zn plating and stripping behavior of the utilized fly ash-coated Zn anode for zinc-ion batteries, Rare Metals (2025). https://doi.org/10.1007/s12598-025-03298-8.

[9] P. Woottapanit, C. Yang, S. Geng, K. Lolupiman, W. Limphirat, X. Zhang, G. He, J. Qin, Electron Donation Effect of α-Boron Nanosheet Enables Highly Stable Zinc Metal Anode, Advanced Functional Materials (2025). https://doi.org/10.1002/adfm.202507725.

1